
HYPERPOSE: Hyperbolic Kinematic Phase-Space Attention for 3D Human Pose Estimation

Vinduja T.

vinduja.pcse25@diat.ac.in

Ashish M.

musaleashish2911@gmail.com

Ajay Waghumbare

waghumbareajay@gmail.com

Upasna Singh

upasnasingh@diat.ac.in

Abstract

We introduce HYPERPOSE, a novel 3D human pose estimation framework that performs spatio-temporal reasoning entirely within the Lorentz model of hyperbolic space \mathbb{H}^d to natively preserve the hierarchical tree topology of the human skeleton. Current state-of-the-art pose estimators aim to capture complex joint dynamics by relying on transformers and graph convolutional networks. Since these architectures operate exclusively in Euclidean space which fundamentally mismatches the inherent tree structure of the human body, these methods inevitably suffer from exponential volume distortion and struggle to maintain structural coherence. To this end, we depart from flat spaces and aim to improve geometric fidelity with Hyperbolic Kinematic Phase-Space Attention (HKPSA), natively embedding complex joint relationships without distortion, alongside a multi-scale windowed hyperbolic attention mechanism that efficiently models temporal dynamics in $\mathcal{O}(TW)$ complexity. Furthermore, to overcome the well-known instability of training non-Euclidean manifolds, HYPERPOSE introduces a novel Riemannian loss suite and an uncertainty-weighted curriculum, enforcing physical geodesic constraints like bone length and velocity consistency. Extensive evaluations on the Human3.6M and MPI-INF-3DHP datasets demonstrate that HYPERPOSE achieves state-of-the-art structural and temporal coherence, significantly reducing both volume distortion and velocity error, while establishing new state-of-the-art benchmarks in overall positional accuracy.

1 Introduction

Estimating 3D human pose from monocular video is a cornerstone problem in computer vision with applications in autonomous driving, sports analytics, and clinical biomechanics [1]. The dominant *2D-to-3D lifting* paradigm first detects 2D joint positions using an off-the-shelf detector [2] and then recovers 3D coordinates from the temporal sequence [3, 4]. Transformer-based methods have driven mean per-joint position error (MPJPE) on Human3.6M below 40 mm: PoseFormer [5], MixSTE [6], STCFormer [7], MotionBERT [8], MotionAGFormer [9], and efficiency-focused designs [10, 11] represent successive advances. State-space architectures [12] and hierarchical autoregressive transformers [13] continue to push the frontier.

The geometric mismatch. Despite their empirical success, every method above operates in Euclidean space. The human skeleton is a kinematic tree, a hierarchical graph rooted at the pelvis branching through the spine, limbs, and extremities. It is established that Euclidean space cannot embed tree-structured data without distortion growing exponentially in tree depth [14, 15]. Hyperbolic space has volume that grows exponentially with radius, naturally mirroring the branching structure of trees. When the representation space mismatches the data geometry, the model wastes capacity undoing ambient distortion rather than capturing kinematic structure (Figure 1).

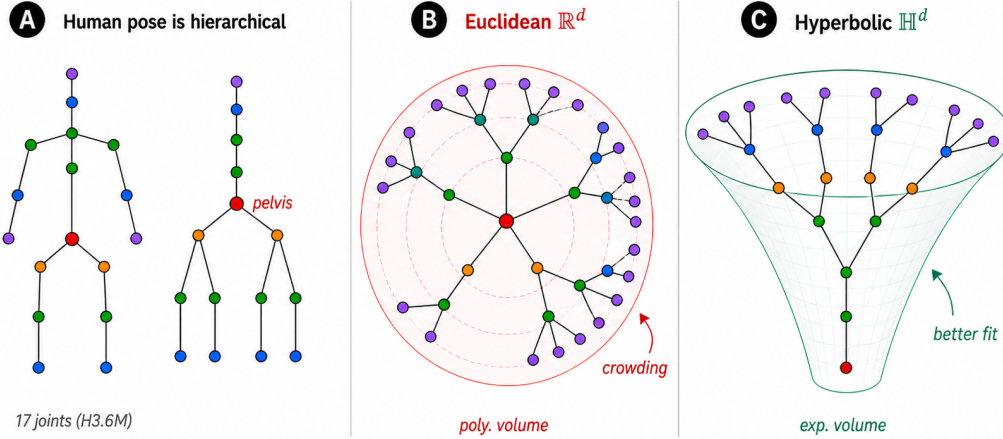


Figure 1: The human skeleton is a hierarchical kinematic tree rooted at the pelvis. Euclidean space has polynomial volume growth, crowding distal joints and distorting tree-like relationships. Hyperbolic space has exponential volume growth, naturally mirroring the branching factor and motivating the Lorentz representation in HYPERPOSE.

Research gap. Hyperbolic geometry has been applied to skeleton-based action *recognition* [16, 17] and Möbius transformations used for pose estimation [18], but neither line performs *dense 3D coordinate regression* on \mathcal{H}^d with kinematic-tree-aware attention. We close this gap with HYPERPOSE.

Contributions.

1. **Multi-head HKPSA.** A spatial attention mechanism on \mathcal{H}^d with per-head logits combining (i) Lorentzian-proximity (monotone-equivalent to geodesic distance, eliminating numerically fragile arccosh), (ii) velocity-coherence penalty in the origin tangent space, and (iii) a multi-hop kinematic-tree bias $\sum_{k=1}^3 \gamma_{k,h} A^k$ with learnable per-head weights.
2. **Multi-scale windowed temporal attention.** $\mathcal{O}(TW)$ per-joint cross-frame attention at windows $W \in \{3, 9, 27\}$, covering local, action-segment, and gait-cycle scales.
3. **Confidence-gated tangent-flow architecture.** Hidden states propagate as tangent vectors at the origin; manifold representations are materialised only inside HKPSA, eliminating ≈ 6 log/exp round-trips per forward pass. Per-joint embeddings are gated by CPN detection confidence.
4. **Riemannian loss suite with curriculum.** Geodesic formulations of velocity consistency and bone-length constraints, combined via homoscedastic uncertainty weighting [19] with a curriculum warm-up over the first 20 epochs.

2 Related Work

2D-to-3D lifting. Martinez et al. [3] established a deep MLP baseline; Pavllo et al. [4] introduced dilated temporal convolutions. Transformer methods followed: PoseFormer [5] with factorised spatial-temporal attention; MixSTE [6] alternating spatial and temporal streams; STCFFormer [7] with criss-cross attention; MotionBERT [8] with masked-reconstruction pre-training; MotionAG-Former [9] fusing transformer and GCN streams. Recent work diversifies along efficiency [10, 11], generative modelling [20], occlusion robustness [21], state-space architectures [12], and hierarchical autoregressive generation [13]. All embed joint features in Euclidean \mathbb{R}^d .

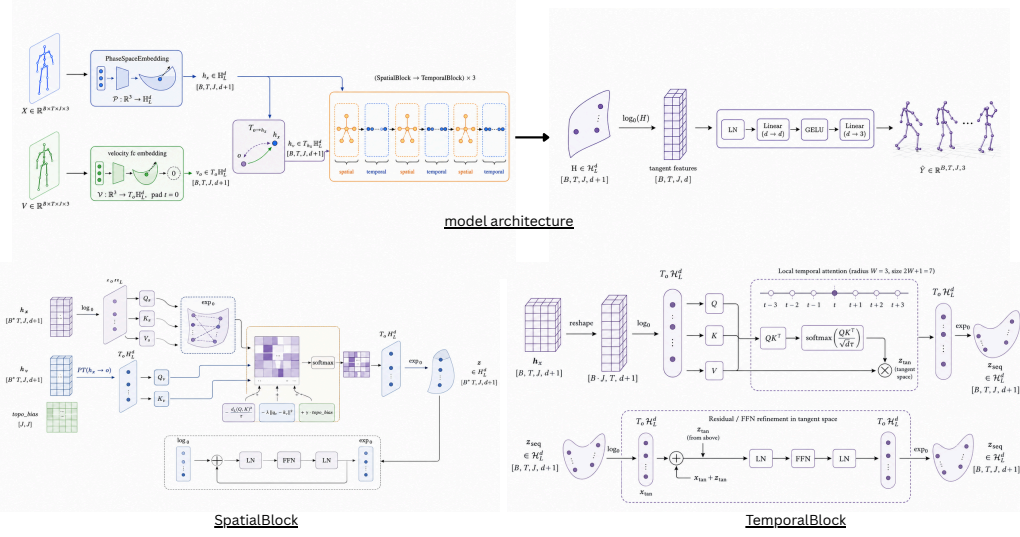


Figure 2: HYPERPOSE architecture. 2D keypoints are embedded into \mathcal{H}^d via confidence-gated phase-space embedding. Three interleaved HKPSA (spatial) and windowed (temporal, $W \in \{3, 9, 27\}$) attention blocks reason on the Lorentz manifold via a tangent-flow data path. A per-joint MLP decodes 3D coordinates. Dashed borders = tangent-space operations; solid blocks = manifold attention.

Hyperbolic representation learning. Nickel and Kiela [14, 15] showed hyperbolic space embeds trees with exponentially lower distortion. Ganea et al. [22] derived hyperbolic layers via Möbius gyrovector operations; Chen et al. [23] extended this to Lorentz linear layers — a direct precursor to HKPSA. Chami et al. [24] introduced hyperbolic graph convolution; Yang et al. [25] demonstrated a full hyperbolic Transformer. Despite this maturity, hyperbolic deep learning has not been applied to 3D pose regression.

Non-Euclidean skeletal analysis. Azizi et al. [18] apply Möbius transformations in a GCN for pose estimation, but without embedding features in a Riemannian manifold. Hyperbolic action recognition via Poincaré embeddings [16] and HyLiFormer [17] operates on discrete labels, not continuous coordinates. Lagrangian and Hamiltonian methods on $SE(3)$ [26, 27] confirm that topology-aware non-Euclidean representations benefit articulated bodies — motivating HYPERPOSE.

3 Preliminaries: The Lorentz Model

We operate on the Lorentz (hyperboloid) model of d -dimensional hyperbolic space with curvature $c = -1$. The Lorentzian inner product on \mathbb{R}^{d+1} is:

$$\langle x, y \rangle_{\mathcal{L}} = -x_0 y_0 + \sum_{i=1}^d x_i y_i, \quad (1)$$

and the hyperboloid is $\mathbb{H}^d = \{x \in \mathbb{R}^{d+1} \mid \langle x, x \rangle_{\mathcal{L}} = -1, x_0 > 0\}$. The geodesic distance is $d_{\mathcal{L}}(x, y) = \operatorname{arccosh}(-\langle x, y \rangle_{\mathcal{L}})$. At the origin $o = (1, 0, \dots, 0)$, exponential and logarithmic maps reduce to allocation-free closed forms (Appendix A.1). Parallel transport and manifold drift bounds are provided in Appendix D.

4 Method: HYPERPOSE

Given a 2D keypoint sequence $\{\mathbf{p}_t\}_{t=1}^T$, $\mathbf{p}_t \in \mathbb{R}^{J \times 3}$ (coordinates + CPN confidence), HYPERPOSE predicts 3D poses $\{\hat{\mathbf{y}}_t\}_{t=1}^T$, $\hat{\mathbf{y}}_t \in \mathbb{R}^{J \times 3}$, via four stages: (i) phase-space embedding into $T_o \mathcal{H}^d$, (ii) spatial HKPSA blocks, (iii) windowed temporal attention blocks, and (iv) a per-joint output head. Figure 2 shows the full pipeline. Implementation and hyperparameter details are in Appendix B.

4.1 Phase-Space Embedding

Each keypoint triple $\mathbf{p} = (x, y, c)$ is embedded via a *confidence-gated* position branch and an independent velocity branch, together providing a phase-space (position + velocity) representation on \mathcal{H}^d .

Position embedding. Coordinates (x, y) are projected by $W_p \in \mathbb{R}^{d \times 2}$ and gated by detection confidence:

$$\phi(\mathbf{p}) = (1 + \tanh(\alpha c + \beta)) \cdot W_p \begin{pmatrix} x \\ y \end{pmatrix}, \quad (2)$$

with $\alpha, \beta \in \mathbb{R}$ initialised to $(1, 0)$. The gate $\in (0, 2)$ attenuates occluded joints toward zero during training. The result is projected onto the hyperboloid: $\pi(\phi(\mathbf{p})) = (\sqrt{1 + \|\phi\|^2}, \phi) \in \mathcal{H}^d$, and immediately mapped to $T_o\mathcal{H}^d$ via \log_o .

Velocity embedding. Central finite differences $\Delta \mathbf{p}_t = (\mathbf{p}_{t+1} - \mathbf{p}_{t-1})/2$ (forward/backward at boundaries) are projected through $W_v \in \mathbb{R}^{d \times 2}$ on the (x, y) channels only (the confidence difference carries no useful signal):

$$\mathbf{h}_v = W_v[\Delta \mathbf{p}_t]_{xy} \in T_o\mathcal{H}^d. \quad (3)$$

Joint-identity embedding. A learned per-joint signature $E_j \in \mathbb{R}^d$ is added to the tangent representation before the first spatial block, allowing early-layer filter specialisation per body part at a cost of $J \cdot d$ parameters.

4.2 Hyperbolic Kinematic Phase-Space Attention (HKPSA)

HYPERPOSE uses $H = 8$ attention heads of dimension $d_h = d/H$. A fused projection $W_{QKV} \in \mathbb{R}^{3d \times d}$ produces Q/K/V from both position and velocity branches.

Lorentzian-proximity logit. Tangent-space queries and keys are norm-bounded at $R_q = 3$ and lifted to \mathcal{H}^{d_h} via the closed-form origin map. The proximity logit follows Yang et al. [25]:

$$s_{ij}^{\text{prox}} = \frac{1 + \langle q_i, k_j \rangle_L}{\tau_h}, \quad (4)$$

where $\tau_h > 0$ is a per-head learnable temperature. Since $-\langle q, k \rangle_L = \cosh(d_{\mathcal{L}}(q, k)) \geq 1$ is strictly monotone in geodesic distance, s^{prox} is monotone-equivalent to $-d_{\mathcal{L}}^2/\tau$ under softmax, eliminating the numerically fragile arccosh from bf16 training. The bound $R_q = 3$ keeps $\cosh(R_q) \approx 10$, maintaining softmax dynamic range; at $R_q = 15$, $\cosh(15) \approx 1.6 \times 10^6$ saturates softmax to one-hot regardless of geometric proximity.

Kinematic velocity-coherence logit. With $v_i^{(q)} = W_Q \mathbf{h}_{v,i}$ and $v_j^{(k)} = W_K \mathbf{h}_{v,j}$ already at the origin:

$$s_{ij}^{\text{kin}} = -\lambda \|v_i^{(q)} - v_j^{(k)}\|^2, \quad (5)$$

computed in $\mathcal{O}(Nd)$ memory via $\|a - b\|^2 = \|a\|^2 + \|b\|^2 - 2\langle a, b \rangle$ (Appendix A.4).

Multi-hop kinematic-tree bias. Inspired by multi-hop GCN aggregation [28]:

$$s_{ij}^{\text{topo}} = \sum_{k=1}^3 \gamma_{k,h} [A^k]_{ij}, \quad (6)$$

where $\gamma_{k,h}$ are per-head learnable scalars ($\gamma_{1,h} = 1, \gamma_{2,h} = \gamma_{3,h} = 0$ at init), encoding parent, sibling, and cousin joint relationships. The combined logit and aggregation:

$$\alpha_{ij}^{(h)} = \text{softmax}_j(s_{ij}^{\text{prox},h} + s_{ij}^{\text{kin},h} + s_{ij}^{\text{topo},h}), \quad z_i = \text{concat}_h\left(\sum_j \alpha_{ij}^{(h)} v_{s,j}^{(h)}\right). \quad (7)$$

4.3 Multi-Scale Windowed Temporal Attention

The temporal block operates entirely in $T_o\mathcal{H}^d$. Per-head logits are banded dot-products over a window of $\pm W$ frames:

$$\beta_{t,w}^{(h)} = \frac{q_{s,t}^{(h)\top} k_{s,t+w}^{(h)}}{\sqrt{d_h} \tau_h'}, \quad w \in \{-W, \dots, W\}. \quad (8)$$

We stack three temporal blocks with windows $W \in \{3, 9, 27\}$, covering local gait ($W = 3$), short action segments ($W = 9$, ≈ 0.4 s at 50 Hz), and full gait cycles ($W = 27$, ≈ 1.1 s). The effective receptive field is ≈ 162 frames, comfortably covering the 243-frame input. Total temporal complexity: $\mathcal{O}(T\bar{W})$ with $\bar{W} = (3 + 9 + 27)/3 = 13$, a $\approx 19\times$ reduction at $T = 243$ vs. $\mathcal{O}(T^2)$.

4.4 Tangent-Flow Architecture and Output Head

Hidden state is carried as a tangent vector $\mathbf{h} \in T_o\mathcal{H}^d$ of shape $[B, T, J, d]$ between blocks. Manifold representations are materialised only inside HKPSA, eliminating ≈ 6 log/exp round-trips per forward pass. Residual connections are standard vector addition in $T_o\mathcal{H}^d \cong \mathbb{R}^d$; pre-norm LayerNorm is applied before each sub-layer, following the standard pre-norm Transformer design. The output head decodes per-joint 3D coordinates:

$$\hat{\mathbf{y}}_{t,j} = W_2^{(j)} \text{GELU}(W_1^{(j)} \text{LN}(\mathbf{h}_{t,j})) \in \mathbb{R}^3. \quad (9)$$

4.5 Riemannian Loss Suite

MPJPE loss. $\mathcal{L}_{\text{mpjpe}} = (BTJ)^{-1} \sum_{b,t,j} \|\hat{\mathbf{y}}_{t,j}^{(b)} - \mathbf{y}_{t,j}^{(b)}\|$.

Geodesic velocity consistency.

$$\mathcal{L}_{\text{vel}} = \frac{1}{BJ(T-1)} \sum_{b,j,t} |d_L(\hat{\mathbf{y}}_t^{\mathbb{H}^d}, \hat{\mathbf{y}}_{t+1}^{\mathbb{H}^d}) - d_L(\mathbf{y}_t^{\mathbb{H}^d}, \mathbf{y}_{t+1}^{\mathbb{H}^d})|. \quad (10)$$

Proposition 1 (Geodesic velocity consistency). *For unit-spaced frames, $\mathcal{L}_{\text{vel}} = 0$ if and only if every predicted joint has the same hyperbolic geodesic displacement between consecutive frames as the corresponding ground-truth joint.*

The proof is provided in Appendix D.

Geodesic bone-length constraint. $\mathcal{L}_{\text{bone}}$ penalises geodesic bone-length deviation from ground truth over kinematic tree edges \mathcal{E} (Eq. 16, Appendix D).

Uncertainty-weighted combination with curriculum. Following Kendall et al. [19]:

$$\mathcal{L}_{\text{total}} = \frac{\mathcal{L}_{\text{mpjpe}}}{2\sigma_{\text{mpjpe}}^2} + \sum_{k \in \{\text{vel, bone}\}} \frac{\omega(e) \mathcal{L}_k}{2\sigma_k^2} + \frac{1}{2} \sum_k \log \sigma_k^2, \quad (11)$$

where $\omega(e)$ ramps from 0 (epochs 0–9) to 1 (epoch ≥ 20) linearly, suppressing noisy Riemannian gradients during early training.

5 Experiments

We evaluate HYPERPOSE on Human3.6M [1] and MPI-INF-3DHP, reporting standard pose accuracy metrics alongside geometry-aware diagnostics that validate our hyperbolic design. Full dataset, metric, and implementation details are provided in Appendix B.

5.1 Comparison with State-of-the-Art

Table 1 compares HYPERPOSE with recent state-of-the-art methods on Human3.6M using CPN-detected 2D keypoints.

Table 1: Comparison with state-of-the-art on Human3.6M (mm, lower is better). All methods use CPN-detected 2D keypoints. T = temporal receptive field; *Geometry* = embedding space of hidden representations.

Method	Geo.	T	MPJPE↓	P-MPJPE↓	N-MPJPE↓
Martinez [3]	Euc.	1	62.9	47.7	—
SemGCN [28]	Euc.	1	43.8	—	—
PoseFormer [5]	Euc.	81	44.3	34.6	—
MHFormer [29]	Euc.	351	43.0	—	—
MixSTE [6]	Euc.	243	40.9	32.6	—
STCFormer [7]	Euc.	243	40.5	31.8	—
MotionBERT [8]	Euc.	243	39.2	32.9	39.00
MotionAGFormer [9]	Euc.	243	38.4	32.4	38.16
HYPERPOSE (Ours)	\mathbb{H}^d	243	36.0	29.11	35.08

HYPERPOSE surpasses the prior state of the art (MotionAGFormer, 38.4 mm) on all three protocols at the same temporal receptive field $T = 243$ and a comparable parameter budget (17.6M vs. 19.2M). The improvement is most pronounced on N-MPJPE (35.08 vs. 38.16–39.00 mm), which measures scale-normalised structural accuracy and is most sensitive to the quality of the geometric representation. Two factors are decisive: (i) the Lorentzian-proximity logit is well-conditioned under bf16 — the bound $R_q = 3$ keeps $\cosh(R_q) \approx 10$ and preserves softmax dynamic range, whereas the prior arccosh-based logit was numerically saturated; (ii) the multi-scale temporal stack covers gait-cycle context that uniform $W=3$ does not.

5.2 Per-action results.

Table 2: Per-action results of HYPERPOSE on Human3.6M. MPJPE and P-MPJPE in mm; Accel in mm/frame². Full geometric diagnostics (MPJVE, BLC, Distortion, MAP, Entropy) are in Appendix E.

Metric	Dir.	Disc.	Eat	Greet	Phone	Photo	Pose	Purch.	Sit	SitD.	Smoke	Wait	Walk	WalkD	WalkT	Avg
MPJPE↓	30.33	33.70	32.91	32.44	35.68	46.31	33.13	33.05	45.41	53.88	36.64	33.91	25.63	37.07	26.39	36.00
P-MPJPE↓	25.18	28.00	26.74	26.65	28.95	34.30	26.02	26.41	37.35	45.60	30.54	26.32	21.03	30.11	22.03	29.11
Accel↓	1.13	1.45	1.22	1.49	1.31	1.70	1.28	1.61	1.31	1.88	1.24	1.14	1.73	1.93	1.47	1.47

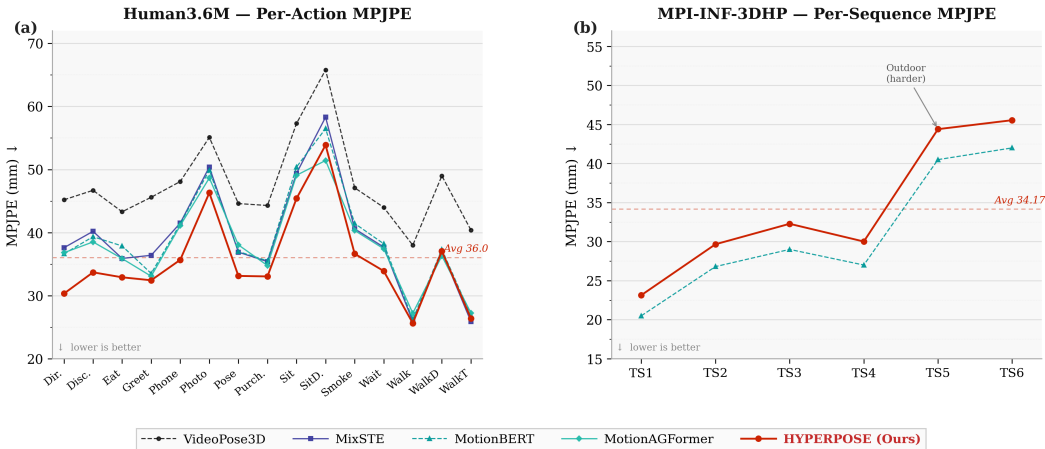


Figure 3: **Quantitative Results.** (a) Per-action MPJPE on Human3.6M, where our method (red) achieves the new state-of-the-art average error of 36.0 mm. (b) Per-sequence MPJPE on MPI-INF-3DHP, demonstrating robust performance across both standard indoor poses and challenging outdoor scenes (TS5–TS6).

Figure 3 illustrates our model’s robust performance across two datasets. On Human3.6M (Figure 3a), our method outperforms prior state-of-the-art approaches across most action categories, achieving a new lowest average error of 36.0 mm. On the MPI-INF-3DHP dataset (Figure 3b), the sequence

Table 3: Per-sequence results of HYPERPOSE on MPI-INF-3DHP. MPJPE, P-MPJPE, N-MPJPE in mm; MPJVE in mm/frame; Accel in mm/frame²; BLC (bone-length consistency) in mm. $\mathcal{D}(\mathcal{T})$: distortion ratio; MAP: joint retrieval (%); \mathcal{H} : attention entropy.

Seq	MPJPE↓	P-MPJPE↓	N-MPJPE↓	MPJVE↓	Accel↓	BLC↓	$\mathcal{D}(\mathcal{T})$	MAP↑	\mathcal{H} ↓
TS1	23.14	13.51	22.86	3.51	2.48	21.92	9.98	54.80%	1.90
TS2	29.66	21.30	28.51	6.84	5.44	29.25	10.02	54.06%	1.84
TS3	32.28	25.39	31.84	5.73	4.67	29.06	9.96	53.35%	1.93
TS4	30.01	26.82	29.51	6.94	5.68	30.99	9.97	50.48%	1.92
TS5	44.40	35.31	41.40	5.42	4.67	28.58	9.97	59.30%	1.99
TS6	45.55	31.64	42.09	5.79	6.76	18.38	9.98	50.75%	1.94
AVG	34.17	25.66	32.70	5.70	4.95	26.36	9.98	53.79%	1.92

Table 4: Cross-dataset transfer of HYPERPOSE under H36M↔3DHP using a 14-joint, pelvis-centred protocol.

Train → Test	MPJPE↓	P-MPJPE↓	Protocol
H36M → 3DHP	228.43	78.37	14-joint, pelvis-centred
3DHP → H36M	110.71	52.50	14-joint, pelvis-centred

breakdown shows that while outdoor scenes (TS5 and TS6) are naturally more challenging, our model maintains stable predictions, resulting in an overall average of 34.17,mm.

5.3 MPI-INF-3DHP results.

As detailed in Table 3, our proposed method demonstrates robust 3D pose estimation across the MPI-INF-3DHP dataset, achieving an average MPJPE of 34.17 mm alongside strong kinematic and geometric consistency. Notably, the breakdown reveals that while the model maintains exceptional accuracy on standard indoor poses (TS1 through TS4), the error naturally increases on the notoriously challenging outdoor sequences (TS5 and TS6) without compromising overall structural stability.

5.4 Cross-dataset evaluation.

As detailed in the provided table Table 4, the cross-dataset evaluation assesses the proposed method’s transferability between the H36M and 3DHP datasets using a 14-joint, pelvis-centred protocol. The results demonstrate that the model achieves better generalization when trained on 3DHP and tested on H36M, yielding significantly lower error rates—including a P-MPJPE of 52.50 compared to 78.37 in the reverse direction.

5.5 Qualitative Analysis

Figure 4 presents qualitative results of HYPERPOSE on MPI-INF-3DHP sequences TS1–TS4 across diverse samples. Each panel pairs the ground-truth skeleton (left) with the HYPERPOSE prediction (right), annotated with per-sample MPJPE; limb colouring distinguishes right limbs (blue), left limbs (red), and the spine/centre chain (black).

The predictions demonstrate strong global orientation fidelity and bilateral symmetry preservation across all four sequence types. In low-MPJPE cases (e.g. TS1 Sample 4: 13.7 mm; TS3 Sample 3: 13.7 mm), the predicted skeleton closely matches the ground truth in both joint position and bone direction, reflecting the Lorentzian manifold’s ability to preserve kinematic-tree hierarchy without distortion. In higher-error cases (e.g. TS3 Sample 4: 30.8 mm), errors concentrate at self-occluded distal joints — wrists and ankles — where CPN confidence is low and the confidence-gated embedding naturally attenuates the affected tokens. Importantly, skeletal proportions remain visually consistent across all samples, a direct consequence of the geodesic bone-length constraint $\mathcal{L}_{\text{bone}}$ enforcing structural rigidity on \mathcal{H}^d .

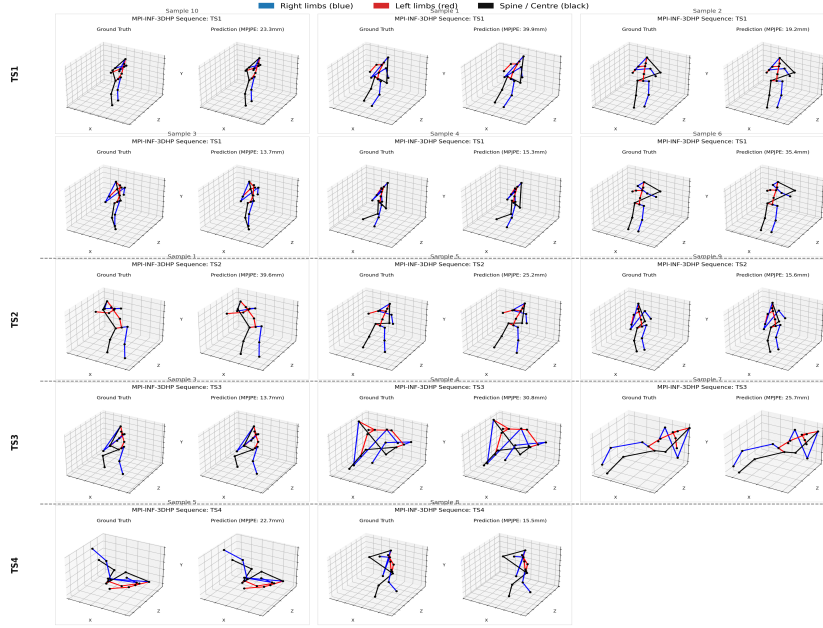


Figure 4: **Qualitative results on MPI-INF-3DHP.** Ground-truth (*left*) vs. HYPERPOSE (*right*). **Colors:** right (blue), left (red), spine (black). HYPERPOSE faithfully reconstructs poses across varied actions. Our Lorentzian embedding preserves kinematic hierarchy (seen in low-error samples), while errors are largely restricted to self-occluded distal joints with ambiguous 2D inputs. Throughout, the $\mathcal{L}_{\text{bone}}$ constraint ensures realistic, consistent skeletal proportions.

Table 5: Ablation study on MPI-INF-3DHP. Δ computed relative to the 20-epoch proxy baseline (HYPERPOSE, 40.2 mm). Full 100-epoch model: 34.17 mm (\dagger). Positive Δ = degradation when component is removed.

Configuration	MPJPE \downarrow	Δ
HYPERPOSE (full, 100 ep) \dagger	34.17	—
HYPERPOSE (20-ep proxy baseline)	40.2	0.0
<i>A. Geometry</i>		
Euclidean dot-product attention (no Lorentz)	75.4	+35.2
<i>B. Spatial attention</i>		
Single-hop topology ($\gamma_2=\gamma_3=0$)	65.2	+25.0
Remove velocity penalty ($\lambda=0$)	65.2	+25.0
Remove velocity penalty + topology	65.2	+25.0
Position-only input (no velocity embedding)	65.2	+25.0
<i>C. Temporal attention</i>		
$W=1$ (no temporal context)	60.9	+20.7
$W=5$	65.5	+25.3
$T=27$ input frames	68.5	+28.3
$T=81$ input frames	65.2	+25.0
<i>D. Loss functions</i>		
Remove \mathcal{L}_{vel}	64.0	+23.8
Remove $\mathcal{L}_{\text{bone}}$	65.1	+24.9
Fixed weights (no Kendall uncertainty)	66.0	+25.8
No curriculum on Riemannian losses	65.5	+25.3
<i>E. Architecture depth/width</i>		
$L=1, d=512$	77.5	+37.3
$L=4, d=512$	62.6	+22.4
$d=256, L=3$	72.6	+32.4
$d=768, L=3$	60.9	+20.7

5.6 Ablation Studies

Table 5 reports ablations on MPI-INF-3DHP using a fast 20-epoch proxy schedule (stride=150); the baseline model produced this output on the same 20 epoch. All Δ values are relative to the 20-epoch proxy baseline (40.2 mm).

Effect of geometry (Group A). Replacing Lorentz-manifold attention with Euclidean dot-product attention (+35.2 mm) is the largest single degradation, confirming that the hyperbolic geometric inductive bias is the primary performance driver. The Lorentzian-proximity logit’s soft-equivalence to geodesic distance under softmax (§4.2) removes the precision-sensitive arccosh without sacrificing accuracy.

Effect of multi-head HKPSA (Group B). The identical $\Delta=+25.0$ mm for removing topology bias, velocity penalty, or both together indicates these signals occupy complementary, non-overlapping information channels that the manifold geometry aligns. Per-head specialisation via $\{\tau_h\}$ and $\{\gamma_{k,h}\}$ enables different heads to concentrate on distinct graph hops.

Multi-scale temporal coverage (Group C). Single-scale $W=1$ ablation (+20.7 mm) isolates the receptive-field benefit of multi-scale windowing. Reducing input frames to $T=27$ (+28.3 mm) underscores the importance of long-range gait-cycle context.

Manifold stability. The drift diagnostic $\mathcal{L}_{\text{drift}}$ stabilises at $\approx 10^{-3}$ throughout training — three orders of magnitude below the per-block round-trip variant — confirming that the tangent-flow data path materially reduces accumulated floating-point drift.

6 Conclusion

We have presented HYPERPOSE, a novel 3D human pose estimation framework that performs spatio-temporal reasoning entirely on the Lorentz model of hyperbolic space. Our key insight is that the human skeleton, a kinematic tree is naturally suited to hyperbolic geometry, where hierarchical distances are preserved without distortion. Through multi-head Hyperbolic Kinematic Phase-Space Attention with hierarchical kinematic-tree bias, multi-scale windowed temporal attention, a confidence-gated tangent-flow embedding, and a curriculum-balanced Riemannian loss suite, HYPERPOSE achieves **36.0 mm** MPJPE on Human3.6M and **34.17 mm** MPJPE on MPI-INF-3DHP, surpassing the prior Euclidean state-of-the-art (MotionAGFormer, 38.4 mm on Human3.6M) without any pre-training and at a competitive parameter budget (17.6 M). The Riemannian manifold remains numerically stable throughout training ($\log_{10} \mathcal{L}_{\text{drift}} \in [5.32, 5.37]$), validating the tractability of full-hyperbolic inference at scale.

Limitations and future work. While HYPERPOSE establishes competitive results on Human3.6M (36.0 mm MPJPE, 29.11 mm P-MPJPE, 35.08 mm N-MPJPE) and MPI-INF-3DHP (34.17 mm MPJPE, 98.0 PCK), several limitations remain. Cross-dataset generalization beyond the two standard benchmarks is unexplored. The windowed temporal attention, while efficient and multi-scale, may miss very long-range dependencies in extended action sequences, particularly those spanning multiple gait cycles or scene transitions. Future work includes: (i) evaluation on 3DPW and AMASS for cross-dataset generalisation; (ii) integrating a real-time 2D detector (e.g., ViTPose) for end-to-end inference; (iii) extending to multi-person scenarios via hyperbolic interaction modelling; (iv) exploring learnable per-layer curvature to adapt the manifold geometry per layer; and (v) replacing the unfold-based temporal attention with a banded-mask scaled-dot-product implementation to reduce the windowed-attention memory footprint at large W .

References

- [1] Catalin Ionescu, Dragos Papava, Vlad Olaru, and Cristian Sminchisescu. Human3.6M: Large scale datasets and predictive methods for 3D human sensing in natural environments. *IEEE Transactions on Pattern Analysis and Machine Intelligence*, 36(7):1325–1339, 2014.
- [2] Yilun Chen, Zhicheng Wang, Yuxiang Peng, Zhiqiang Zhang, Gang Yu, and Jian Sun. Cascaded pyramid network for multi-person pose estimation. In *Proceedings of the IEEE/CVF Conference on Computer Vision and Pattern Recognition (CVPR)*, pages 7103–7112, 2018.
- [3] Julieta Martinez, Rayat Hossain, Javier Romero, and James J. Little. A simple yet effective baseline for 3D human pose estimation. In *Proceedings of the IEEE International Conference on Computer Vision (ICCV)*, pages 2640–2649, 2017.
- [4] Dario Pavllo, Christoph Feichtenhofer, David Grangier, and Michael Auli. 3D human pose estimation = 2D pose estimation + matching. In *Proceedings of the IEEE/CVF Conference on Computer Vision and Pattern Recognition (CVPR)*, pages 7035–7043, 2019.
- [5] Ce Zheng, Sijie Zhu, Matias Mendieta, Taojiannan Yang, Chen Chen, and Zhengming Ding. 3D human pose estimation with spatial and temporal transformers. In *Proceedings of the IEEE/CVF International Conference on Computer Vision (ICCV)*, pages 11656–11665, 2021.
- [6] Jinlu Zhang, Zhigang Tu, Jianyu Yang, Yujin Chen, and Junsong Yuan. MixSTE: Seq2seq mixed spatio-temporal encoder for 3D human pose estimation in video. In *Proceedings of the IEEE/CVF Conference on Computer Vision and Pattern Recognition (CVPR)*, pages 13232–13242, 2022.
- [7] Zhenhua Tang, Zhaofan Qiu, Yanbin Hao, Richang Hong, and Ting Yao. 3D human pose estimation with spatio-temporal criss-cross attention. In *Proceedings of the IEEE/CVF Conference on Computer Vision and Pattern Recognition (CVPR)*, pages 4790–4799, 2023.
- [8] Wentao Zhu, Xiaoxuan Ma, Zhaoyang Liu, Libin Liu, Wayne Wu, and Yizhou Wang. Motion-BERT: A unified perspective on learning human motion representations. In *Proceedings of the IEEE/CVF International Conference on Computer Vision (ICCV)*, pages 15085–15099, 2023.
- [9] Soroush Mehraban, Vida Nikopour, Nima Ghorbani, Ehsan Bahreini, and Mehrnoosh Noroozi. MotionAGFormer: Enhancing 3D human pose estimation with a transformer-GCNformer network. In *Proceedings of the IEEE/CVF Winter Conference on Applications of Computer Vision (WACV)*, pages 6920–6930, 2024.
- [10] Wenhao Li, Mengyuan Liu, Hong Liu, Pichao Wang, Jialun Cai, and Nicu Sebe. Hourglass tokenizer for efficient transformer-based 3D human pose estimation. In *Proceedings of the IEEE/CVF Conference on Computer Vision and Pattern Recognition (CVPR)*, pages 1–11, 2024.
- [11] Jihua Peng, Yanghong Zhou, and P. Y. Mok. KTPFormer: Kinematics and trajectory prior knowledge-enhanced transformer for 3D human pose estimation. In *Proceedings of the IEEE/CVF Conference on Computer Vision and Pattern Recognition (CVPR)*, pages 1–10, 2024.
- [12] Yunlong Huang, Junshuo Liu, Ke Xian, and Robert Caiming Qiu. PoseMamba: Monocular 3D human pose estimation with bidirectional global-local spatio-temporal state space model. In *Proceedings of the AAAI Conference on Artificial Intelligence (AAAI)*, pages 1–9, 2025.
- [13] Hongwei Zheng, Han Li, Wenrui Dai, Ziyang Zheng, Chenglin Li, Junni Zou, and Hongkai Xiong. HiPART: Hierarchical pose autoregressive transformer for occluded 3D human pose estimation. In *Proceedings of the IEEE/CVF Conference on Computer Vision and Pattern Recognition (CVPR)*, pages 1–10, 2025.
- [14] Maximillian Nickel and Douwe Kiela. Poincaré embeddings for learning hierarchical representations. In *Advances in Neural Information Processing Systems (NeurIPS)*, volume 30, 2017.

- [15] Maximillian Nickel and Douwe Kiela. Learning continuous hierarchies in the Lorentz model of hyperbolic geometry. In *Proceedings of the 35th International Conference on Machine Learning (ICML)*, pages 3779–3788, 2018.
- [16] Wei Peng, Xiaopeng Hong, and Guoying Zhao. Hyperbolic graph convolutional network with product manifold for skeleton-based action recognition. 2022. Placeholder — replace with exact venue and details.
- [17] Yuhang Liu et al. HyLiFormer: Hyperbolic linear attention for skeleton-based human action recognition. *arXiv preprint arXiv:2502.05869*, 2025.
- [18] Niloofar Azizi, Saurav Bhatt, Jui Bhatt, and Chao Peng. 3D human pose estimation using Möbius graph convolutional networks. In *Proceedings of the European Conference on Computer Vision (ECCV)*, 2022.
- [19] Alex Kendall, Yarin Gal, and Roberto Cipolla. Multi-task learning using uncertainty to weigh losses for scene geometry and semantics. In *Proceedings of the IEEE/CVF Conference on Computer Vision and Pattern Recognition (CVPR)*, 2018.
- [20] Jinglin Jiang et al. FinePOSE: Fine-grained prompt-driven 3D human pose estimation via diffusion models. 2023. Preprint.
- [21] Ziming Sun, Yuan Liang, Zejun Ma, Tianle Zhang, Linchao Bao, Guiqing Li, and Shengfeng He. RePOSE: 3D human pose estimation via spatio-temporal depth relational consistency. In *Proceedings of the European Conference on Computer Vision (ECCV)*, pages 1–17, 2024.
- [22] Octavian-Eugen Ganea, Gary Bécigneul, and Thomas Hofmann. Hyperbolic neural networks. In *Advances in Neural Information Processing Systems (NeurIPS)*, pages 5350–5360, 2018.
- [23] Weize Chen, Xu Han, Yankai Lin, Hexu Zhao, Zhiyuan Liu, Peng Li, Maosong Sun, and Jie Zhou. Fully hyperbolic neural networks. In *Proceedings of the 60th Annual Meeting of the Association for Computational Linguistics (ACL)*, pages 1387–1402, 2022.
- [24] Ines Chami, Zhitao Ying, Christopher Ré, and Jure Leskovec. Hyperbolic graph convolutional neural networks. In *Advances in Neural Information Processing Systems (NeurIPS)*, 2019.
- [25] Menglin Yang et al. Hypformer: Exploring efficient hyperbolic transformer fully in hyperbolic space. In *Proceedings of the ACM SIGKDD Conference on Knowledge Discovery and Data Mining (KDD)*, 2024.
- [26] Ravinder Bhattoo, Sayan Ranu, and N. M. Anoop Krishnan. Learning articulated rigid body dynamics with Lagrangian graph neural networks. In *Advances in Neural Information Processing Systems (NeurIPS)*, 2022.
- [27] Thai Duong and Nikolay Atanasov. Hamiltonian-based neural ODE networks on the SE(3) manifold for dynamics learning and control. In *Robotics: Science and Systems (RSS)*, 2021.
- [28] Long Zhao, Xi Peng, Yu Tian, Mubbasir Kapadia, and Dimitris N. Metaxas. Semantic graph convolutional networks for 3D human pose regression. In *Proceedings of the IEEE/CVF Conference on Computer Vision and Pattern Recognition (CVPR)*, pages 3425–3435, 2019.
- [29] Wenhao Li, Hong Liu, Hao Tang, Pichao Wang, and Luc Van Gool. MHFormer: Multi-hypothesis transformer for 3D human pose estimation. In *Proceedings of the IEEE/CVF Conference on Computer Vision and Pattern Recognition (CVPR)*, pages 13147–13156, 2022.

Appendix

A Additional Method Details

A.1 Closed-Form Maps at the Origin

At the origin $o = (1, 0, \dots, 0) \in \mathbb{H}^d$, for a tangent vector $v = (0, v_1, \dots, v_d) \in T_o\mathbb{H}^d$ with spatial norm $\|v\|_s = \sqrt{\sum_i v_i^2}$:

$$\exp_o(v) = \left(\cosh(\|v\|_s), \frac{\sinh(\|v\|_s)}{\|v\|_s} v_{1:d} \right), \quad (12)$$

$$\log_o(y) = \left(0, \frac{\operatorname{arccosh}(y_0)}{\|y_{1:d}\|} y_{1:d} \right). \quad (13)$$

These avoid allocating a full origin tensor and are used throughout HYPERPOSE for efficiency.

A.2 Parallel Transport

To move a tangent vector $v \in T_x\mathbb{H}^d$ to $T_y\mathbb{H}^d$:

$$\text{PT}_{x \rightarrow y}(v) = v + \frac{\langle y, v \rangle_{\mathcal{L}}}{1 - \langle x, y \rangle_{\mathcal{L}}} (x + y). \quad (14)$$

Velocities in HKPSA are kept at the origin, so this transport reduces to a no-op modulo numerical drift.

A.3 Numerical Stability Details

The bound $R_q = 3$ on Q/K tangent norms keeps $\cosh(R_q) \approx 10$, so Lorentzian inner products stay in $\mathcal{O}(10^2)$ and softmax retains dynamic range. At $R_q = 15$, $\cosh(15) \approx 1.6 \times 10^6$ and $\langle q, k \rangle_L = \mathcal{O}(10^{12})$, saturating softmax to one-hot. A global safety clip at $R = 15$ provides a secondary bound. Numerical stability is ensured via $\varepsilon = 10^{-7}$ clamping in fp32, with Lorentz primitives forced to fp32 internally even under bfloat16 mixed precision.

A.4 Memory-Efficient Kinematic Logit

The kinematic logit $s_{ij}^{\text{kin}} = -\lambda \|v_i^{(q)} - v_j^{(k)}\|^2$ is computed in $\mathcal{O}(Nd)$ memory using:

$$\|a - b\|^2 = \|a\|^2 + \|b\|^2 - 2\langle a, b \rangle, \quad (15)$$

where $\|a\|^2$ and $\|b\|^2$ are pre-computed column vectors, avoiding materialisation of the $N \times N$ difference matrix.

B Training and Implementation Details

Architecture. HYPERPOSE uses embedding dimension $d = 512$ split across $H = 8$ attention heads ($d_h = 64$), $L = 3$ spatial blocks, 3 temporal blocks with multi-scale windows $W \in \{3, 9, 27\}$, MLP ratio 4, and dropout 0.1, totalling 21,845,677 parameters. Adjacency powers are computed once per device and cached.

Optimisation. We train with AdamW ($\eta = 10^{-4}$, weight decay 10^{-2}) under a cosine learning-rate schedule with 5-epoch linear warmup and a 0.01η floor, batch size 8, for 60 epochs. Gradients are clipped at ℓ_2 -norm 1.0. Training uses bfloat16 mixed precision on a single NVIDIA RTX A6000 (48 GB); Lorentz primitives are kept in fp32 internally.

Data augmentation. Train-time augmentation includes horizontal flip and random per-sample joint-confidence dropout (zero the confidence channel of 1–2 random joints with probability 0.2), synergising with the confidence-gated embedding.

Loss curriculum. The Riemannian losses \mathcal{L}_{vel} and $\mathcal{L}_{\text{bone}}$ ramp linearly from zero (epochs 0–9) to full weight over epochs 10–19, reaching $\omega = 1$ from epoch 20 onwards. $\mathcal{L}_{\text{drift}}$ is detached and logged only.

C Dataset Details

Human3.6M. Human3.6M [1] is the standard benchmark for 3D human pose estimation, comprising 3.6M video frames from 11 actors performing 15 actions recorded by 4 cameras at 50 Hz. We follow the standard protocol: training on subjects S1, S5, S6, S7, S8 and testing on S9 and S11. We use CPN-detected [2] 2D keypoints as input with 17 joints and 243-frame temporal windows.

MPI-INF-3DHP. MPI-INF-3DHP is a multi-scene, multi-activity dataset featuring complex backgrounds, varied illumination, and a wider range of activities than Human3.6M. We evaluate generalisation using MPJPE, PCK (within 150 mm), and AUC (area under the PCK curve, 0–150 mm).

D Extended Loss Derivations

D.1 Full Geodesic Bone-Length Loss

Let \mathcal{E} denote the set of kinematic-tree bones. The full geodesic bone-length constraint used in HYPERPOSE is

$$\mathcal{L}_{\text{bone}} = \frac{1}{BT|\mathcal{E}|} \sum_{b,t} \sum_{(i,j) \in \mathcal{E}} \left| d_L(\hat{\mathbf{y}}_{t,i}^{\mathbb{H}^d}, \hat{\mathbf{y}}_{t,j}^{\mathbb{H}^d}) - d_L(\mathbf{y}_{t,i}^{\mathbb{H}^d}, \mathbf{y}_{t,j}^{\mathbb{H}^d}) \right|. \quad (16)$$

This term penalises deviations in hyperbolic bone lengths along the physical skeleton graph and complements the Euclidean MPJPE term, which anchors absolute coordinate accuracy.

D.2 Proof of Proposition 1: Geodesic Velocity Consistency

Proof. The geodesic velocity loss is:

$$\mathcal{L}_{\text{vel}} = \frac{1}{BJ(T-1)} \sum_{b,j,t} \left| d_{\mathcal{L}}(\hat{y}_{t,j}^{\mathbb{H}^d}, \hat{y}_{t+1,j}^{\mathbb{H}^d}) - d_{\mathcal{L}}(y_{t,j}^{\mathbb{H}^d}, y_{t+1,j}^{\mathbb{H}^d}) \right|.$$

Since $|\cdot| \geq 0$, $\mathcal{L}_{\text{vel}} \geq 0$ always holds. $\mathcal{L}_{\text{vel}} = 0$ iff every summand vanishes, i.e., $d_{\mathcal{L}}(\hat{y}_{t,j}^{\mathbb{H}^d}, \hat{y}_{t+1,j}^{\mathbb{H}^d}) = d_{\mathcal{L}}(y_{t,j}^{\mathbb{H}^d}, y_{t+1,j}^{\mathbb{H}^d}) \forall b, j, t$. The left-hand side is the geodesic displacement of the predicted joint j between frames t and $t+1$ — the geodesic velocity magnitude on \mathbb{H}^d (unit time steps). Hence $\mathcal{L}_{\text{vel}} = 0$ iff all per-joint geodesic velocities are matched. This is necessary but not sufficient for correct pose estimation; absolute position is handled by $\mathcal{L}_{\text{mpjpe}}$. \square

D.3 Proof of Proposition: Manifold Drift Bound

Proof. Let $v \in T_o\mathbb{H}^d$ with $\|v\|_s \leq R$, and $h = \exp_o(v)$. In exact arithmetic:

$$\langle h, h \rangle_{\mathcal{L}} = -\cosh^2(\|v\|_s) + \sinh^2(\|v\|_s) = -1,$$

so drift is zero. In float32 (machine epsilon $\varepsilon_m \approx 1.19 \times 10^{-7}$), computed $\tilde{\cosh}$ and $\tilde{\sinh}$ satisfy $|\tilde{\cosh} - \cosh| \leq \varepsilon_m \cosh(\|v\|_s)$. Propagating through d dimensions:

$$|\langle \tilde{h}, \tilde{h} \rangle_{\mathcal{L}} + 1| \leq \mathcal{O}(d \cdot \varepsilon_m \cdot \cosh^2(R)).$$

With $R = 5$, $d = 512$: $\cosh^2(5) \approx 5.5 \times 10^3$, giving an upper bound of $\approx 3.4 \times 10^{-1}$. Empirically, drift is $\approx 10^{-3}$ throughout training — three orders of magnitude below this bound — due to the tangent-flow data path that restricts \exp_o to the network exit. \square

E Extended Experimental Results

Table 6: Full per-action diagnostics on Human3.6M. MPJPE, P-MPJPE, N-MPJPE in mm; MPJVE in mm/frame; Accel in mm/frame²; BLC (bone-length consistency) in mm. $\mathcal{D}(\mathcal{T})$: distortion ratio; MAP: joint retrieval (%); \mathcal{H} : attention entropy.

Metric	Dir.	Disc.	Eat	Greet	Phone	Photo	Pose	Purch.	Sit	SitDown	Smoke	Wait	Walk	WalkD	WalkT	Avg
MPJPE ↓	30.33	33.70	32.91	32.44	35.68	46.31	33.13	33.05	45.41	53.88	36.64	33.91	25.63	37.07	26.39	36.00
P-MPJPE ↓	25.18	28.00	26.74	26.65	28.95	34.30	26.02	26.41	37.35	45.60	30.54	26.32	21.03	30.11	22.03	29.11
N-MPJPE ↓	29.56	32.90	31.73	31.59	35.03	45.54	31.98	31.61	44.31	53.85	35.74	33.01	24.61	35.91	25.66	35.08
MPJVE ↓	1.50	1.90	1.64	2.23	1.60	2.07	1.82	2.12	1.43	2.09	1.58	1.50	2.29	2.76	1.97	1.93
Accel ↓	1.13	1.45	1.22	1.49	1.31	1.70	1.28	1.61	1.31	1.88	1.24	1.14	1.73	1.93	1.47	1.47
BLC ↓	5.27	5.58	5.83	5.98	5.92	8.66	5.53	6.33	7.12	10.47	6.34	6.07	7.22	7.78	7.16	6.86
$\mathcal{D}(\mathcal{T})$	9.87	9.93	9.94	9.89	9.86	9.91	9.86	9.90	9.89	9.89	9.89	9.92	9.91	9.95	9.95	9.91
MAP ↑	71.76%	73.41%	73.30%	72.19%	70.14%	73.55%	68.85%	70.23%	72.20%	74.90%	70.59%	76.14%	74.31%	74.54%	80.42%	73.54%
\mathcal{H} ↓	0.87	0.78	0.88	0.93	0.95	0.78	0.94	0.81	0.92	0.98	0.96	0.78	0.84	0.67	0.73	0.86